Electronic properties of asymmetrically doped twisted graphene bilayers

Guy Trambly de Laissardière,[1,*] Omid Faizy Namarvar,[2,†] Didier Mayou,[3,4,‡] and Laurence Magaud[3,4,§]

[1]*Laboratoire de Physique Théorique et Modélisation, CNRS, Université de Cergy-Pontoise, F-95302 Cergy-Pontoise, France*

[2]*CEMES CNRS, 29 rue Jeanne Marvig, F-31055 Toulouse, France*

[3]*Université Grenoble Alpes, Institut Neel, F-38042 Grenoble, France*

[4]*CNRS, Institut Neel, F-38042 Grenoble, France*

(Received 15 March 2016; revised manuscript received 31 May 2016; published 20 June 2016)

Rotated graphene bilayers form an exotic class of nanomaterials with fascinating electronic properties governed by the rotation angle θ. For large rotation angles, the electron eigenstates are restricted to one layer and the bilayer behaves like two decoupled graphene layers. At intermediate angles, Dirac cones are preserved but with a lower velocity and van Hove singularities are induced at energies where the two Dirac cones intersect. At very small angles, eigenstates become localized in peculiar moiré zones. We analyze here the effect of an asymmetric doping for a series of commensurate rotated bilayers on the basis of tight-binding calculations of their band dispersions, density of states, participation ratio, and diffusive properties. While a small doping level preserves the θ dependence of the rotated bilayer electronic structure, larger doping induces a further reduction of the band velocity in the same way as a further reduction of the rotation angle.

DOI: 10.1103/PhysRevB.93.235135

I. INTRODUCTION

What remains really surprising with graphene is that all these outstanding electronic and mechanical properties come from a system that is one atomic layer thick [1–3]. Few-layer graphene and more precisely bilayers also present fascinating properties. It has been known for years that in this case, stacking plays a crucial role. While AA bilayers (all C atoms are in the same position in the two layers) result in two Dirac cones shifted in energy, AB stacking, as in graphite, breaks the atom A/atom B symmetry and leads to a quadratic dispersion [4–8]. Here, we focus on exotic bilayers that present neither AA nor AB stacking but with a relative rotation of the two layers.

Different approaches are used nowadays to obtain graphene: mechanical peeling of graphite, annealing of SiC, CVD on metals. These three approaches also give multilayers with, in some cases, a rotation between successive layers. Indeed, rotated bilayers have been obtained on graphite but also on Ni and on the C face of SiC. A rotation between two layers creates a (pseudo)periodicity that appears as a moiré pattern on STM images [9–12]. All the theoretical works [13–30] now agree on the fact that two graphene layers stacked with a rotation between them show exotic electronic properties that are angle dependant. The AA and AB stackings are the two extreme cases: they correspond to rotations of 0° and 60°. The bilayer behavior is symmetric with respect to a rotation angle equal to 30°. At large angles (close to 30°), the two layers are decoupled and behave like independent graphene planes. At smaller angles, graphene Dirac cones are conserved but the velocity is renormalized (reduced). Van Hove singularities (vHs) are found at energies where the Dirac cones from the two layers intersect [31–34]. Eventually, for small angles the two vHs merge at the Dirac energy and give a sharp peak in the density of states (DOS). The corresponding states are localized in a region of the supercell where stacking is close to AA [23,24].

Here, we check the robustness of the theoretical predictions with respect to doping which can be an important perturbation. Indeed, bilayers often show an asymmetric doping, one layer more doped than the other one, either the doping is made on purpose if a potential bias is applied between the layers or it results from charge transfer with a substrate. In a tight-binding (TB) scheme, an asymmetric doping is a shift in electrochemical potential between the two layers. An asymmetric doping opens a gap in the band structure of an AB bilayer. We will show that it is not the case for rotated bilayers and that for not too small angles and reasonable doping, linear dispersion, velocity renormalization, and vHs remain. The main effect of doping is to shift one Dirac cone with respect to the other one by an energy that varies with the doping rate and the rotation angle. Localization of the states either on one layer (large angle, decoupled layers) or on both but in AA regions (small angles) is not drastically changed by doping. The complex electronic structure of graphene bilayers is a consequence of the local geometry of the system. A parallel can be drawn with quasicrystals where the quasicrystals specific properties develop when the size of the approximant cell increases [35–37]. In the same way, here specific properties arise when the commensurate cell size increases and the AA and AB regions are better defined. The parallel is obvious when one looks at transport properties and the importance of the non-Boltzmann part either for neutral or doped bilayers.

The numerical method and atomic structures of rotated bilayer are detailed in Sec. II and in the Appendix, then the effect of doping on the band structure (Sec. III), average velocity (Sec. IV), and the density of states (Sec. V) are discussed. The participation ratios are convenient quantity to characterize the states repartition as a function of the energy. It is shown for neutral and doped bilayer in Sec. VI. Finally, specific quantum diffusion due to confined states in doped and undoped twisted graphene bilayers is presented Sec. VII. For

*guy.trambly@u-cergy.fr
†omid.faizy@cemes.fr
‡didier.mayou@neel.cnrs.fr
§laurence.magaud@neel.cnrs.fr

TABLE I. Studied (n,m) bilayer structures. N is the number of atoms, θ the rotation angle, and $V_x/V_{\rm m}$ the undoped rotated bilayer velocity at K point along the x direction divided by the monolayer velocity [24].

(n,m)	θ (°)	N	$V_x/V_{\rm m}$
(1,3)	32.20	52	0.99
(5,9)	18.73	604	0.99
(2,3)	13.17	76	0.96
(3,4)	9.43	148	0.95
(6,7)	5.08	508	0.83
(8,9)	3.89	868	0.74
(12,13)	2.65	1876	0.48
(15,16)	2.13	2884	0.35
(25,26)	1.30	7804	0.02
(33,34)	0.99	13468	0.01

comparison, quantum diffusion in graphene is presented in the Appendix.

II. NUMERICAL METHODS AND ATOMIC STRUCTURE

Tackling small rotation angles (smaller than 4°) means handling very large cells that can involve a huge number of atoms, i.e., more than 10 000 (Table I). We use a tight-binding (TB) scheme developed [23,24] for p_z orbitals since we are interested in what happens at energies within ±2 eV of $E_{\rm D}$, the Dirac point energy whatever the rotation angle is. The TB scheme is described in details in Ref. [24]. Since the planes are rotated, neighbors are not on top of each other (as it is the case in the Bernal AB stacking). Interlayer interactions are then not restricted to $pp\sigma$ terms but some $pp\pi$ terms have also to be introduced. The Hamiltonian has the form

$$\hat{H} = \sum_i \epsilon_i \, |i\rangle\langle i| + \sum_{\langle i,j\rangle} t_{ij} \, |i\rangle\langle j|, \tag{1}$$

where $|i\rangle$ is the p_z orbital with energy ϵ_i located at $\vec{r}_i$, and $\langle i,j\rangle$ is the sum on index i and j with $i \neq j$. The coupling matrix element t_{ij} between two p_z orbitals located at $\vec{r}_i$ and $\vec{r}_j$ is [38]

$$t_{ij} = \langle i|\hat{H}|j\rangle = n_c^2 V_{pp\sigma}(r_{ij}) + \left(1-n_c^2\right) V_{pp\pi}(r_{ij}), \tag{2}$$

where n_c is the direction cosine, $V_{pp\sigma}$ and $V_{pp\pi}$ the Slater-Koster coupling parameters. In our scheme [24], $V_{pp\sigma}$ and $V_{pp\pi}$ are exponentially decaying function of the distance. It is known that the results of the band calculations are sensitive to a particular form of these parameters, and different parametrizations of the Slater-Koster coupling parameters are used in the literature [29,30]. However, many general aspects of the band structure in rotated twisted bilayer are found similarly with different TB parametrizations. Asymmetric doping is modeled using different onsite energies on the two layers. All orbitals of a layer have the same energy. In the following, results are given as a function of the potential bias $\Delta\epsilon$ between the two layers. $\Delta\epsilon$ is the difference between the onsite energies $\epsilon_1 = \epsilon_0$ on the top and the onsite energies $\epsilon_2 = \epsilon_0 - \Delta\epsilon$ on the bottom layers. The coupling beyond first neighbor induces an asymmetry between states above and below the Dirac energy in each layer. All energies are then given with respect to the Dirac energy E_{D1} of the top undoped layer (top layer) which is set to zero.

The eigenstates obtained by diagonalization in reciprocal space of the TB Hamiltonian are used to calculate transport characteristic values (velocity, square spreading, diffusivity) as explained in the Appendix. In monolayer graphene (Appendix 3), transport properties are well described by the usual semiclassical Boltzmann approach (excepted at Dirac energy), but in twisted bilayer with small rotation angle θ, very unusual effects occur at Dirac energy that are not taken into account by Boltzmann approach (Sec. VII). The average densities of states in each layer are presented briefly in Sec. V. They are calculated by recursion method in real space starting from a random phases state [39]. This method gives total DOSs that are similar to the one obtained by diagonalization in reciprocal space.

Our calculations require periodic boundary conditions. The way a bilayer supercell is built and how it is labeled (n,m) is described in Refs. [23,24]. We start from an AA bilayer and choose the rotation origin O at an atomic site. A commensurate structure can be defined if the rotation changes a lattice vector $\overrightarrow{OB}(m,n)$ to $\overrightarrow{OB'}(n,m)$, where the integers n, m are the coordinates with respect to the basis vectors $\vec{a}_1$ $(\sqrt{3}a/2,-a/2)$ and $\vec{a}_2$ $(\sqrt{3}a/2,a/2)$, with $a = 0.2456$ nm. The rotation angle is then defined by

$$\cos\theta = \frac{n^2+4nm+m^2}{2(n^2+nm+m^2)}, \tag{3}$$

and the commensurate cell vectors correspond to

$$\vec{t} = \overrightarrow{OB'} = n\vec{a}_1 + m\vec{a}_2\,, \quad \vec{t}' = -m\vec{a}_1 + (n+m)\vec{a}_2. \tag{4}$$

The commensurate unit cell contains $N = 4(n^2+nm+m^2)$ atoms. It is now well established [14,22–27] that the rotation angle θ is a good parameter to describe the system, but the number of atoms is not since cells of equivalent size can be found for different angles. For θ values less than ∼15°, twisted bilayer forms a moiré pattern with (pseudo)period P [40]:

$$P = \frac{a}{2\sin(\theta/2)} \simeq \frac{1.42}{\theta(\rm deg)} \text{ in nm}. \tag{5}$$

Structures of the bilayers studied in this paper are listed in Table I.

III. BAND DISPERSIONS

A. Large and intermediated angles

An asymmetrically doped bilayer with a bernal stacking presents a gap due to the break of all atom A/atom B symmetry. But in twisted bilayer, the situation is completely different [41]. A schematic diagram of the asymmetrically doped rotated bilayer is given in Fig. 1. It applies to the large and intermediate angle cases which still show two Dirac cones. The small angle limit is more complex because of the important state mixing between the two layers. As a consequence of the asymmetric doping, one Dirac cone is shifted and intersection between bands no longer occurs at the midpoint between K_1 and K_2, as it was the case in neutral systems. Then, the maximum of the band (and then the van Hove singularity at E_+ and E_-,

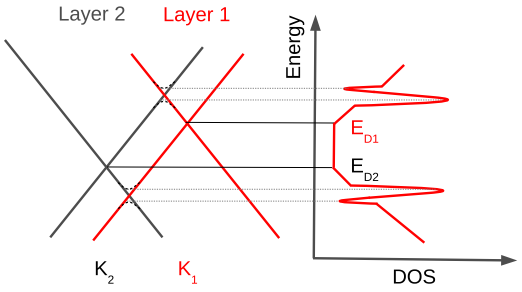

FIG. 1. Dirac cones and total DOS of a doped rotated bilayer, schematic diagram.

see Sec. V) is no longer located at point M of the supercell Brillouin zone (Figs. 2 and 3). No gap opens even for large doping ($\Delta\epsilon = 0.6$ eV and even more). For a given doping, the energy difference $\Delta E_D = E_{D1} - E_{D2}$ between the two Dirac points varies with the rotation angle which results from

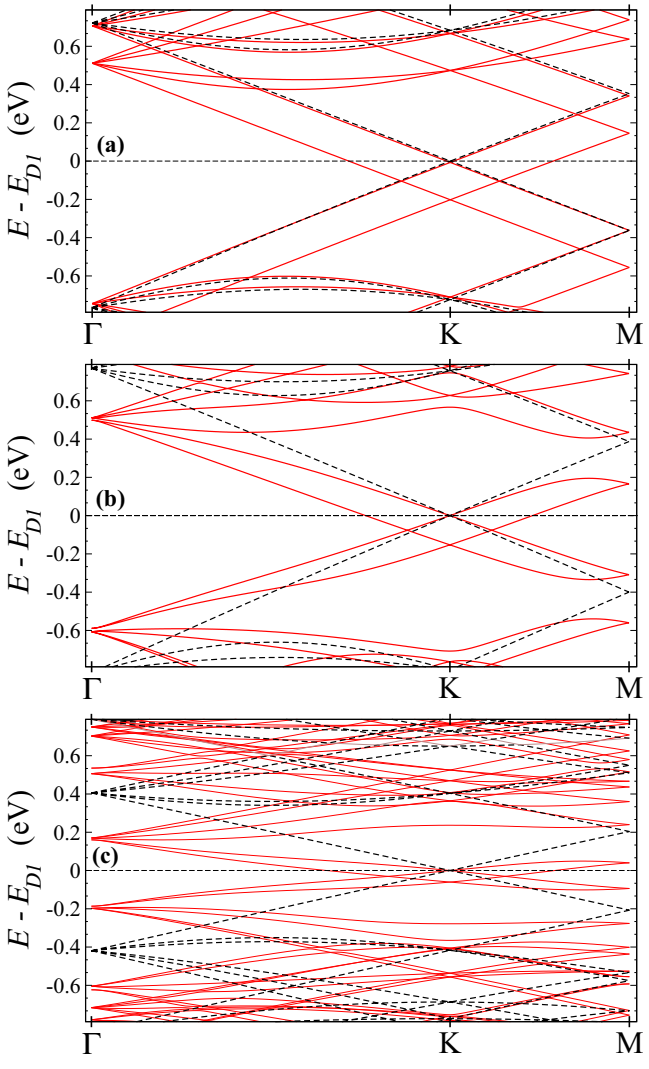

FIG. 2. Band dispersions for doped bilayers with $\Delta\epsilon = 0.2$ eV. (a) (5,9) bilayer ($\theta = 18.73°$), (b) (6,7) bilayer ($\theta = 5.08°$), and (c) (12,13) bilayer ($\theta = 2.65°$). Lines (dashed line) are TB calculations for bilayers (monolayer).

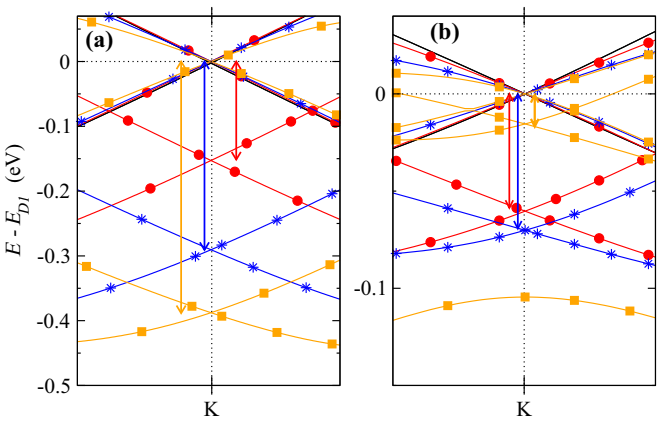

FIG. 3. Band dispersions for doped bilayers: (a) (6,7) bilayer ($\theta = 5.08°$), (b) (12,13) bilayer ($\theta = 2.65°$). The onsite energy difference $\Delta\epsilon$ between p_z orbitals in the two layers is (solid line) $\Delta\epsilon = 0$, (circle) $\Delta\epsilon = 0.2$ eV, (star) $\Delta\epsilon = 0.4$ eV, (square) $\Delta\epsilon = 0.6$ eV. Arrows show the energy difference ΔE_D between bands at **K** (Table II). $E(\vec{k})$ has been computed for more then 50 $\vec{k}$ values in the k scale shown in these figures.

interplane state mixing. These energy differences are shown by arrows on Fig. 3 and they are given in Table II.

Considering the two Dirac cones in reciprocal space (Fig. 1), whatever the values of $\Delta\epsilon > 0$ and of θ are, TB calculations show that the bands of the shifted Dirac cone never cross the bands of the nonshifted Dirac cone. Then, $\Delta E_D(\Delta\epsilon)$ has a maximum ΔE_{Dm} for every θ value (see the inset of Fig. 4). This limit ΔE_D value, corresponding to $\Delta\epsilon = \Delta\epsilon_m$, is always found when one branch of the shifted Dirac cone approaches the parallel branch of the second cone [$\Delta E_D(\Delta\epsilon_m) = \Delta E_{Dm}$]. If doping is small enough, $\Delta\epsilon < \Delta\epsilon_m$, the energy difference ΔE_D between the Dirac cones increases with the onsite energy differences $\Delta\epsilon$. The increase factor is smaller for smaller angles. If doping is larger, $\Delta\epsilon > \Delta\epsilon_m$, ΔE_D decreases when doping increases (Fig. 4). For each angle θ, the maximum value can be understood in a

TABLE II. Energy bands splitting ΔE_D at K point in doped (n,m) bilayers. $\Delta\epsilon$ is the onsite energy difference between p_z orbitals in the two layers.

(n,m)	$\Delta\epsilon$ (eV)	ΔE_D (eV)
(5,9)	0.2	0.20
	0.4	0.40
	0.6	0.60
(3,4)	0.5	0.45
	1.0	0.87
	1.25	1.00
(6,7)	0.2	0.15
	0.4	0.29
	0.6	0.39
(12,13)	0.2	0.06
	0.4	0.07
	0.6	0.02
(25,26)	0.2	0.011
	0.4	0.004

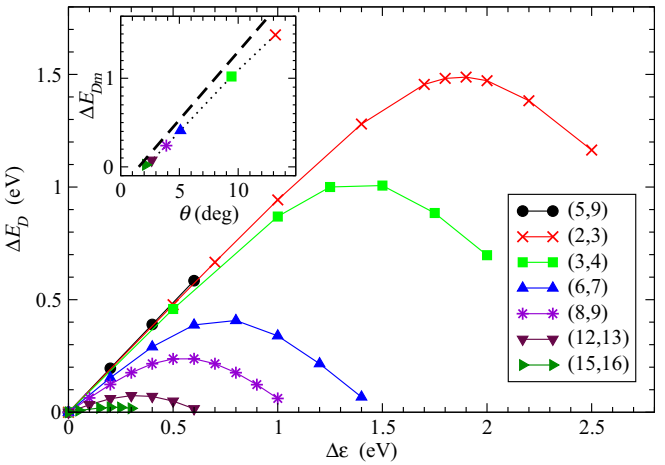

FIG. 4. ΔE_D versus $\Delta\epsilon$ in rotated doped bilayers. [Inset: maximum value ΔE_{Dm} of ΔE_D versus the θ angle. Points line is guide for the eyes. The dashed lines show $\Delta E_{\rm vHs}$ given by Eq. (7), i.e., here $\Delta E_{\rm vHs} \simeq 0.15\,\theta$ (deg) $- 0.24$.]

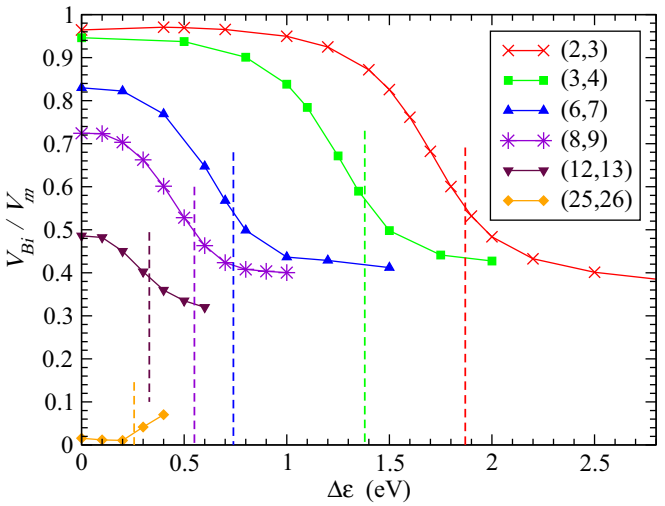

FIG. 5. Velocity at Dirac point (slope of the band along KM at K and Dirac energy) versus $\Delta\epsilon$ in rotated doped bilayers. The vertical dashed lines show the values $\Delta\epsilon_m$ for which $\Delta E_D(\Delta\epsilon)$ is maximum.

simple scheme as follows. For small doping (small $\Delta\epsilon$), it is obvious that

$$\Delta E_D \leqslant \Delta E_{Dm} < \Delta E_{\rm vHs} = E_+ - E_-. \quad (6)$$

This condition is satisfied for any doping (at least for doping that preserves the existence of Dirac cone). From continuum model [14,25,26,31], experimental measurements [33,34], and our calculations (Sec. V), the energy of van Hove singularity is

$$\Delta E_{\rm vHs} = \hbar v_F K_1 K_2 - 2t_\theta = 2\hbar v_F \Gamma K \sin(\theta/2) - 2t_\theta \quad (7)$$

for angles larger than $\sim 2^\circ$. Where v_F is the Fermi velocity for monolayer graphene, $\Gamma K = 1.703$ Å^{-1} is the wave vector of Dirac point in monolayer graphene, and t_θ is the modulus of the amplitude of the main Fourier compoments of the interlayer potential $t_\theta \simeq 0.12$ eV [24,27]. The calculated maximum value of ΔE_D is drawn in the inset of Fig. 4, showing that condition (6) is satisfied. It is interesting to remark also that for (n,m) bilayer, such as $|m-n| > 1$ for instance (5,9) in Fig. 4, when $\Delta\epsilon$ increases a mixing of bands could occur before the maximum value of ΔE estimated by the condition (6).

For doping small enough, $\Delta\epsilon \ll \Delta\epsilon_m$, slopes of the band dispersions $E(k)$ at Dirac point are not modified [Figs. 2(a), 2(b), and 3(a)]. But, for larger $\Delta\epsilon$ values, this slope decreases as $\Delta\epsilon$ increases, which results in a strong reduction of the intraband velocity at Dirac points. Figure 5 shows this renormalization for different θ values. Above this limit [Figs. 2(c) and 3(b)] $\Delta\epsilon > \Delta\epsilon_m$, bands become flatter and intraband velocity reaches a limit value $\sim 0.4 V_{\rm mono}$ (Fig. 5). Therefore, for large rotation angles and physically reasonable doping ($\Delta\epsilon \ll \Delta\epsilon_m$), the velocity renormalization [14,18,19,22–28] is not modified; but, for intermediate rotation angles, actual doping can lead to strong velocity renormalization.

B. Very small angles

The case of very small angles, typically for $\theta <\sim 2^\circ$, is illustrated on Figs. 5 and 6 for different doping values in (25,26) bilayer. The two Dirac cones at E_{D1} and E_{D2} are still present and the maximum value of ΔE_D is obtained for $\Delta\epsilon_m \simeq 0.25$ eV (Fig. 6), but the behavior of intraband velocity at K point versus $\Delta\epsilon$ differs from that for intermediate and large angles (Fig. 5), showing that a new regime is obtained. Bands with energy E around Dirac energies are very flat and states at these energies are not only those of Dirac cones at K points. Therefore, the velocity of electrons at these energies is the average of velocity of all states $\vec{k}$ at energy $E(\vec{k}) = E$ as discussed in the next section.

IV. AVERAGE INTRABAND VELOCITY

The average intraband velocity (Bloch-Boltzamnn velocity) is calculated numerically from the velocity operator $\hat{V}_x$ along the x direction and Eq. (A8) as explained in the Appendix. It is shown in Fig. 7 for several (n,m) bilayers. As expected, for large rotated angles and small doping, this method gives velocity values that are similar to those calculated directly from the slope of bands $E(\vec{k})$ of Dirac cone (intraband velocity at K shown in Fig. 5). For intermediate angles [Fig. 7(b)], the effect of the renormalization of the intraband velocity at K points is seen, but this effect is small because other bands contribute also to the average velocity at same energies. For very small angles [Fig. 7(c)], a very small average velocity is obtained at Dirac energy (confined states), with velocity similar to the intraband value at K points. This renormalization effect remains strong for doped bilayers but energies of localized states (small velocity) are shifted. This strong reduction of the intraband velocity has consequences on electronic transport properties as shown in Sec. VII.

V. DENSITY OF STATES

The shift of one Dirac cone in doped bilayers induces a modification in the DOS as schematically shown in Fig. 1. The van Hove singularities (vHs) are not at the M point of the supercell Brillouin zone but fall somewhere on the K-M line. Furthermore, the DOS is constant in-between the two

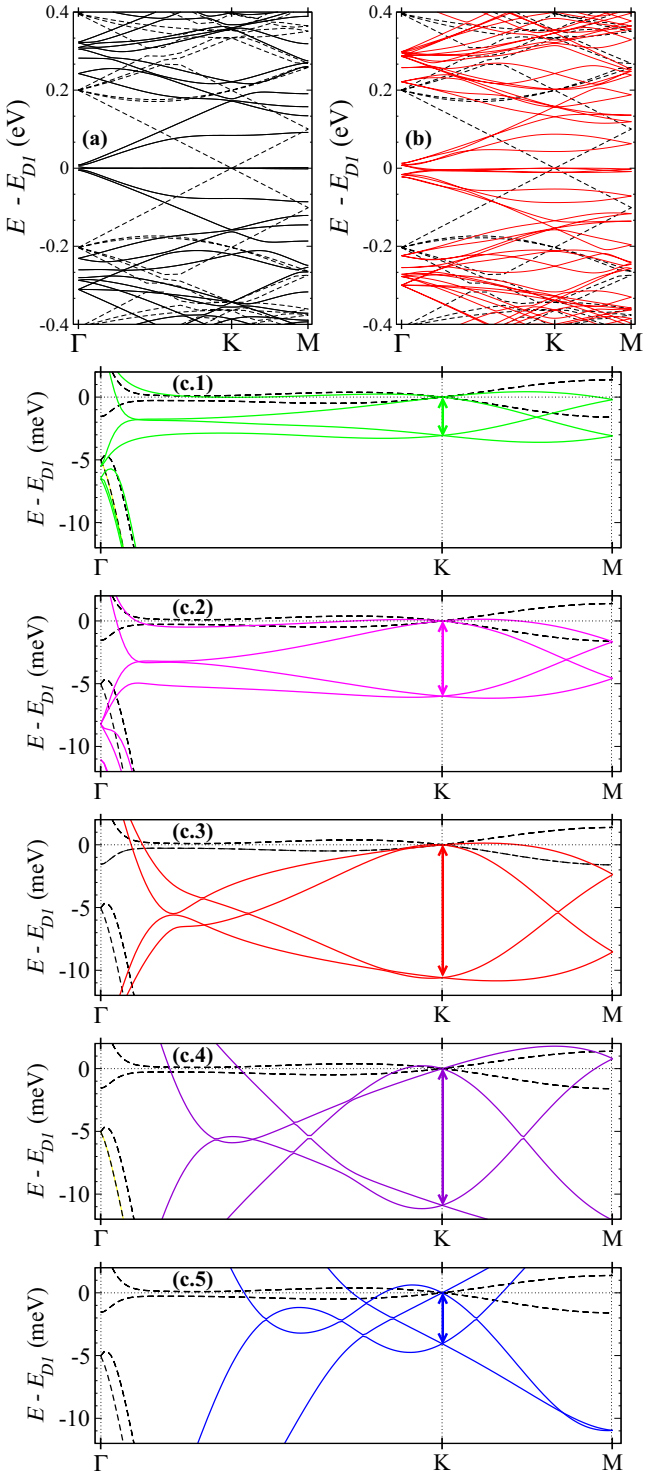

FIG. 6. Band dispersions for (25,26) bilayer ($\theta = 1.30°$): (a) undoped bilayer ($\Delta\epsilon = 0$), (b) doped bilayer $\Delta\epsilon = 0.2$ eV. (c) Zoom around energy E_{D1}: (dashed line) $\Delta\epsilon = 0$, (c.1) $\Delta\epsilon = 0.05$ eV, (c.2) $\Delta\epsilon = 0.1$ eV, (c.3) $\Delta\epsilon = 0.2$ eV, (c.4) $\Delta\epsilon = 0.3$ eV, (c.5) $\Delta\epsilon = 0.4$ eV. The arrows show the energy difference ΔE_D.

Dirac cones, as it is for this energy range in a AA bilayer. These two characteristics are found on the DOS of bilayers with large and intermediate angles [Figs. 8(a) and 8(b)]. For realistic doping and not too small rotation angles, the variations

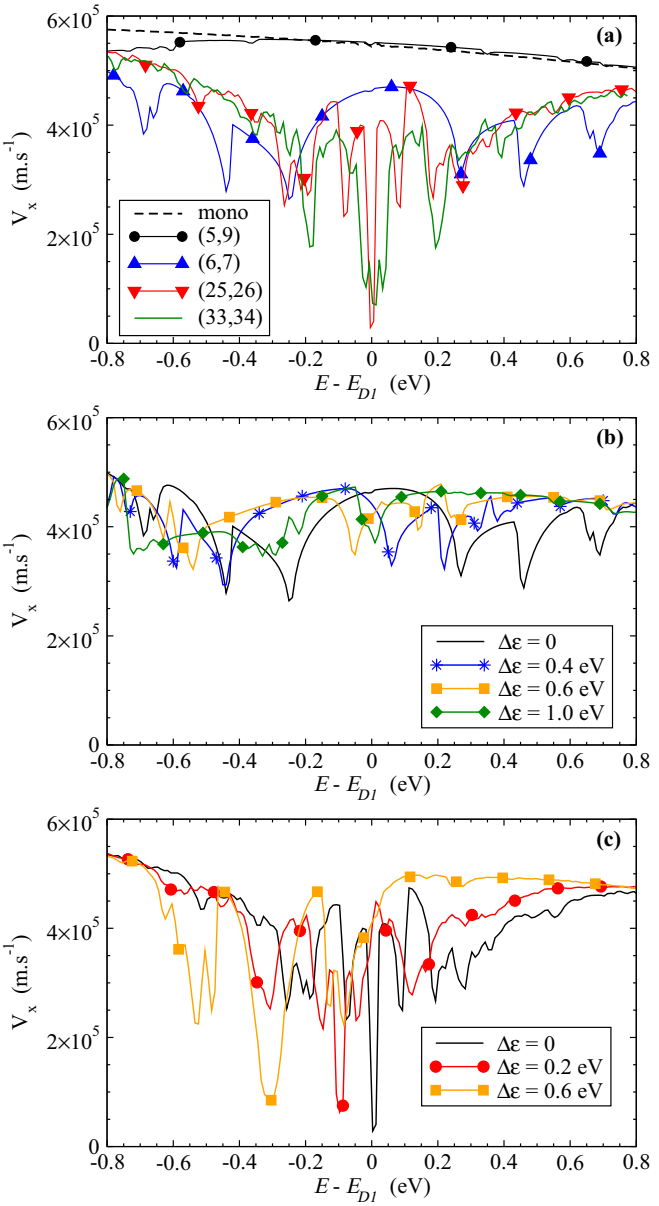

FIG. 7. Average velocity V_x along the x axis ($V = \sqrt{2}V_x$) versus energy E. (a) (Dashed line) graphene and undoped (n,m) bilayers ($\Delta\epsilon = 0$). (b) (6,7) bilayer and (c) (25,26) bilayer: (solid line) undoped ($\Delta\epsilon = 0$), (circle) $\Delta\epsilon = 0.2$ eV, (star) $\Delta\epsilon = 0.4$ eV, and (square) $\Delta\epsilon = 0.6$ eV.

of the vHs energies difference ΔE_{vHs}, $\Delta E_{\text{vHs}} = E_+ - E_-$, with the rotation angle are very similar to those of undoped bilayers [Fig. 8(e)], as recently found from scanning tunneling spectroscopy by Cherkez *et al.* [34]. For very small angles, the localization in AA zone of the moiré is still present and the sharp peak in the DOS is shifted [Figs. 8(d) and 7(c)].

DOSs in each layer of doped bilayers are presented Fig. 9 for intermediate and small rotation angles. As expected, the global shape of DOS in doped layer is shifted in energy by the doping. In any cases, the peaks of vHs or the peak of localization around Dirac energy are clearly seen in the two-layer DOSs at the same energies. This suggests that corresponding states are spread in the two layers as shown in the next section.

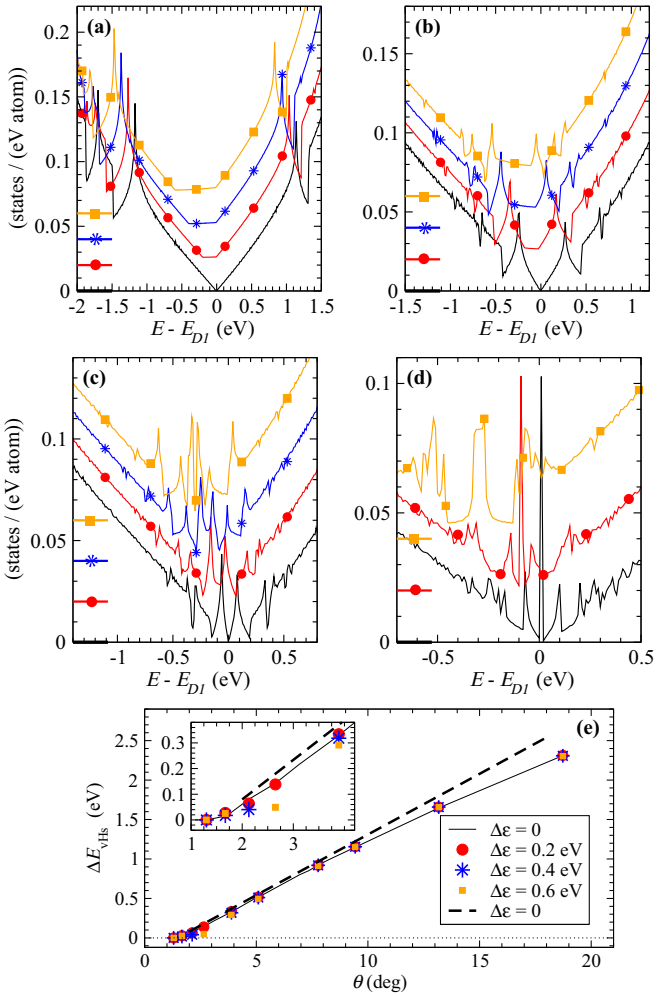

FIG. 8. Total density of states (DOS) in (a) (5,9), (b) (6,7), (c) (12,13), and (d) (25,26) bilayers. The onsite energy difference $\Delta\epsilon$ between p_z orbitals in the two layers is (solid line) $\Delta\epsilon = 0$, (circle) $\Delta\epsilon = 0.2$ eV, (star) $\Delta\epsilon = 0.4$ eV, (square) $\Delta\epsilon = 0.6$ eV. The DOS curves have been shifted vertically for clarity (the origin of the DOS for each curve is indicated by the horizontal line on the lower left corner). (e) Energy difference between the energies $\Delta E_{\rm vHs}$ of vHs, $\Delta E_{\rm vHs} = E_+ - E_-$, versus rotation angle for different doping values. The fine solid line is guide for the eye. Dashed line shows $\Delta E_{\rm vHs}$ given by Eq. (7), i.e., here $\Delta E_{\rm vHs}({\rm eV}) \simeq 0.15\,\theta({\rm deg}) - 0.24$.

VI. PARTICIPATION RATIO

To analyze the nature of the eigenstates in the bilayers and search for a possible doping effect, we compute the participation ratio of each TB eigenstate $|\psi\rangle$ defined by

$$p(\psi) = \frac{1}{N \sum_i |\langle i|\psi\rangle|^4}\,, \tag{8}$$

where $|i\rangle$ are the p_z orbitals on atoms i and N is the number of atoms in a unit cell. For a completely delocalized eigenstate, p is equal to 1 as in graphene. If the state is restricted to one graphene layer, p is equal to 0.5 and a state localized on 1 atom has the smallest p value: $p = 1/N$. The average participation ratio $\langle p\rangle$ as a function of the energy E is presented on Fig. 10(a) for neutral bilayers and Figs. 11(a)–11(d) for doped ones.

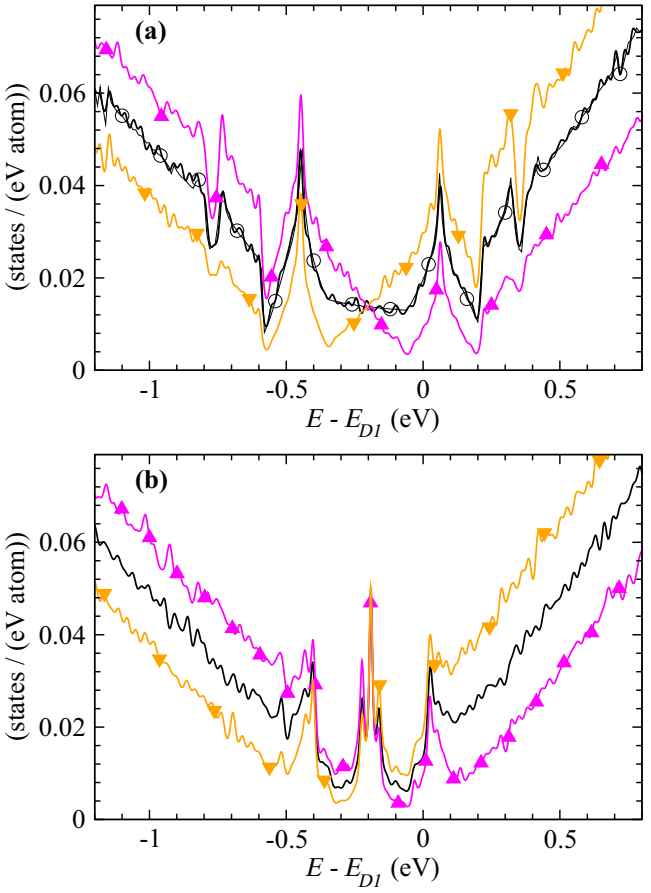

FIG. 9. Density of states (DOS) calculated by recursion in doped (a) (6,7), (b) (25,26) bilayers with $\Delta\epsilon = 0.4$ eV: (solid line) total DOS, (triangle up) average DOS in layer 1 (undoped layer), (triangle down) average DOS in layer 2 (doped layer). (a) The total DOS in (6,7) bilayer, calculated by diagonalization in reciprocal lattice, is also shown with fine line with empty circle. It is very close with total DOS calculated by recursion method.

The participation ratios for neutral systems clearly illustrate the three regimes of the electronic structure of twisted bilayers as a function of the rotation angle through the behavior of the eigenstates.

For large angles θ [bilayers (1,3) ($\theta = 32.20°$) and (5,9) ($\theta = 18.73°$) in Fig. 10(a)], $\langle p\rangle$ is equal to 0.5 which means that the eigenstate is delocalized on one of the two layers. The layers are then decoupled in agreement with the different predictions [13–15,17–19,22–24,27]. Doping does not affect this result as shown Fig. 11(a) for (5,9) bilayer.

For intermediate θ values [bilayers (6,7) ($\theta = 5.08°$) in Fig. 11(b) and (12,13) ($\theta = 2.65°$) in Fig. 11(c)], the participation ratio of a state slightly depends on the energy. It is closer to one in the energy range of the vHs where the interaction between the two planes is stronger and closer to 0.5 in the vicinity of the Dirac energy (interaction between layers is smaller for these energies). When the bilayer is doped, the energy region where the interaction between planes is weaker is just shifted accordingly.

For very small θ values [bilayer (25,26) ($\theta = 1.30°$) in Figs. 10 and 11(d) and (33,34) ($\theta = 0.99°$)], states with energy

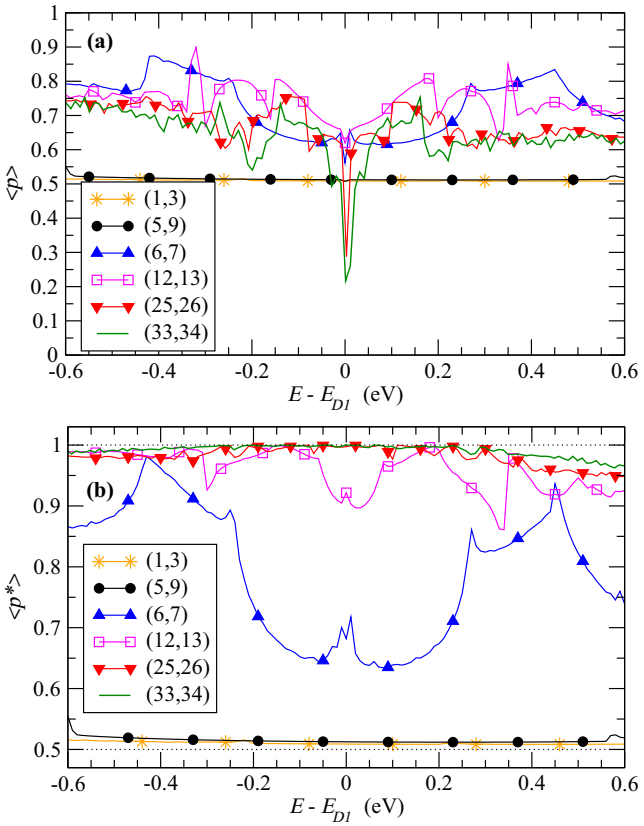

FIG. 10. TB (a) average participation ratio and (b) average layer participation ratio in (n,m) undoped bilayers ($\Delta\epsilon = 0$).

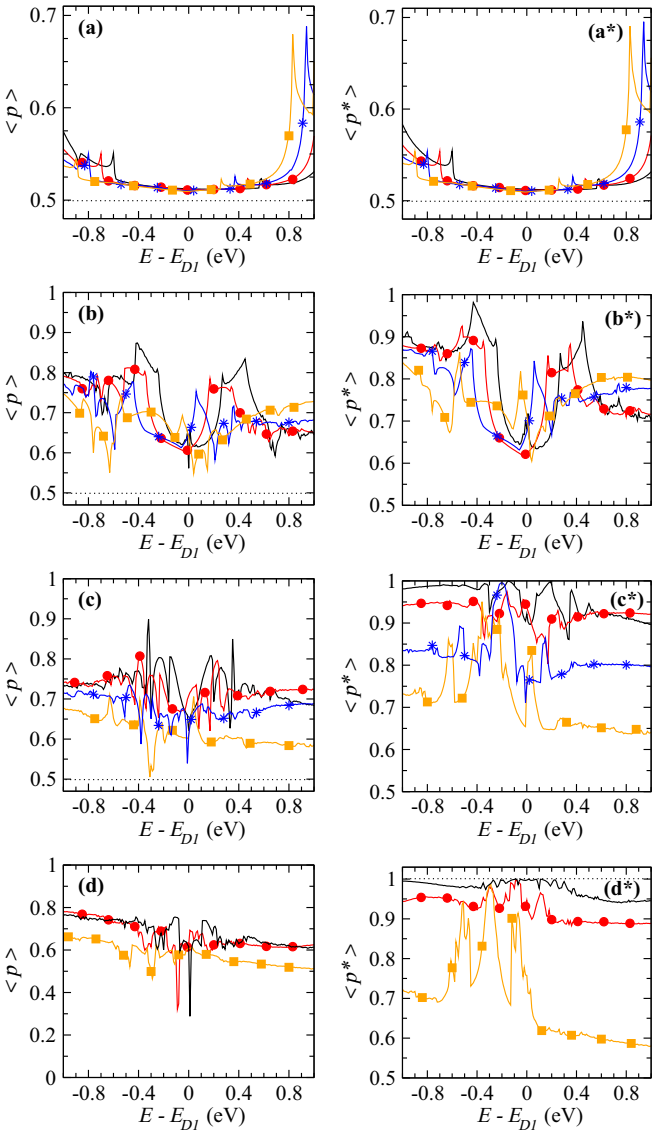

FIG. 11. TB average participation ratio $\langle p\rangle$ and average layer participation ratio $\langle p\rangle^*$ in (a) (5,6), (b) (6,7), (c) (12,13), and (d) (25,26) bilayers. The onsite energy difference $\Delta\epsilon$ between p_z orbitals in the two layers is (black line) $\Delta\epsilon = 0$, (circle) $\Delta\epsilon = 0.2$ eV, (star) $\Delta\epsilon = 0.4$ eV, (square) $\Delta\epsilon = 0.6$ eV.

around 0 are strongly localized (small $\langle p\rangle$ values). An analysis of spatial repartition of eigenstates shows that theses states are localized on the AA zones of the moiré (see Refs. [23,24]). For instance, the participation ratio of one eigenstate at Dirac point is $p \simeq 0.12$ in (33,34) [23]. The peak remains but shifted in the doped case [Fig. 11(d)].

We also define a participation ratio per layer by

$$p^*(\psi) = \frac{1}{2\left(P_1^2 + P_2^2\right)}, \tag{9}$$

where P_l, $l = 1$ and 2 are the weight of the eigenstate ψ on layers 1 and 2, respectively:

$$P_l = \sum_{i_l} |\langle i_l|\psi\rangle|^2, \tag{10}$$

where $|i_l\rangle$ are the p_z orbitals on the atoms i_l of the layer l. An eigenstate with nonzero weight only in one layer corresponds to $p^* = \frac{1}{2}$, whereas $p^* = 1$ for an eigenstate uniformly delocalized on the two layers. The average layer participation ratio $\langle p^*\rangle$ at energy E is presented on Fig. 10(b) for neutral bilayers and Figs. 11(a)*–11(d*) for doped ones. For large θ angles, states exist only in one of the two layers ($\langle p^*\rangle \simeq \frac{1}{2}$) whatever the doping is [Figs. 10(b) and 11(a*)]. As θ decreases, $\langle p^*\rangle$ increases, which shows that states spread more and more on the two layers. For very small θ, states of undoped cases are uniformly distributed on the two layers for all energies [Fig. 10(b)]. Figure 10(b) also shows that for intermediate angles, the distribution of eigenstate on the two layers is weaker close to the Dirac energy than for energy in the vicinity of the vHs. For intermediated θ and very small θ, higher doping also seems to decrease the distribution on the two layers [Figs. 11(c*) and 11(d*)].

While doping does not change qualitatively the average participation ratio $\langle p\rangle$, it significantly decreases the average participation ratio per layer $\langle p^*\rangle$. Therefore, an asymmetric doping in a rotated bilayer favors a decoupling of the states between the layers. For very small angles [Figs. 11(d) and 11(d*), $\theta = 1.30°$], the localization in the AA zone is obtained in the doped as in the undoped bilayer. At all energies around Dirac energy, states are distributed on the two layers $0.9 \leqslant \langle p^*\rangle \leqslant 1$, and the doping reduces a little bit the equal repartition of each eigenstate between the two layers in undoped bilayer $\langle p^*\rangle$(doped) $< \langle p^*\rangle$(undoped) $\simeq 1$.

VII. QUANTUM DIFFUSION IN BILAYERS

In this section, we analyze the consequence on transport properties of the "localization" mechanism [17–19,23,24,42] induced by the small rotation angles. The conductivity along the x axis is given by the Einstein formula

$$\sigma_{xx}(E_{\rm F}) = \frac{e^2}{S} n(E_{\rm F}) \mathcal{D}(E_{\rm F}), \tag{11}$$

where $n(E_{\rm F})$ and $\mathcal{D}(E_{\rm F})$ are the total density of states per surface S and the average diffusivity at the Fermi energy $E_{\rm F}$, respectively. In the relaxation time approximation [35,43,44], the effect of disorder is taken into account by a scattering time τ. In this approach, τ contains both elastic scattering times τ_e due to static defects (adatoms, vacancies,...) and inelastic scattering time τ_i due to phonons or magnetic field (...): $\tau^{-1} = \tau_e^{-1} + \tau_i^{-1}$. τ decreases when the temperature T increases and when the concentration of static defects increases. As explained in the Appendix, the diffusivity $\mathcal{D}$ can by determined at every energy E as function of the scattering time τ. $\mathcal{D}$ is the sum of two terms

$$\mathcal{D}(E_{\rm F},\tau) = \mathcal{D}_{\rm B}(\tau) + \mathcal{D}_{\rm NB}(E_{\rm F},\tau), \tag{12}$$

where $\mathcal{D}_{\rm B}(E_{\rm F},\tau) = V_B^2\tau/3$ is the Boltzmann term and $\mathcal{D}_{\rm NB}$ the non-Boltzmann term. $\mathcal{D}_{\rm NB}$ comes from nondiagonal terms in the velocity operator [Eq. (A7) in the Appendix]. In crystals, it is related to interband transitions activated by elastic or inelastic scattering. For large τ, $\mathcal{D}_{\rm NB}$ decreases when τ increases, and $\mathcal{D}_{\rm NB} \to 0$ when $\tau \to +\infty$. Thus, in crystals, $\mathcal{D} \simeq \mathcal{D}_{\rm B}$ when $\tau \to +\infty$.

Diffusivity calculated for graphene and several bilayers is presented in Fig. 12 for different $E_{\rm F}$ values and for doped or undoped bilayers. For graphene and bilayers with large and intermediate rotation angles, $\mathcal{D} \simeq \mathcal{D}_{\rm B}$ at every energy. The only effect of non-Boltzmann term is a change in the slope of $\mathcal{D}(\tau)$ at scattering time $\tau \simeq \hbar/E$ as explained in the Appendix. Eventually, at small scattering time $\tau \ll \hbar/E$, the interband transition between the two bands of each Dirac cone contributes significantly. In the case of graphene, with a first-neighbor coupling Hamiltonian, the non-Boltzmann term $\mathcal{D}_{\rm NB}$ is equal to Boltzmann term $\mathcal{D}_{\rm B}$ and then $\mathcal{D} = 2\mathcal{D}_{\rm B}$ for $\tau \ll \hbar/E$ [see Eqs. (A14) and (A15) in Appendix 3]. This effect is related with the phenomenon of jittery motion also called Zitterbewegung [3] which is important in the optical conductivity. In graphene and bilayers with large rotated angles, it occurs for very small scattering time values to be significant experimentally. But, in rotated bilayers with very small rotation angle θ, for states at energy where velocity is very small (i.e., energies close to Dirac energy), the Boltzmann term in Eq. (12) goes down and the non-Boltzmann term becomes significant in the total diffusivity. For instance, Fig. 12(a) shows that for (25,26) bilayers ($\theta = 1.3^\circ$) at $E_{\rm F} = 0$, $\mathcal{D}$ is strongly affected by the non-Boltzmann term for realistic [45] τ values. It results in a smaller diffusivity with respect to the graphene case, that is almost independent on scattering time for $\tau \simeq 10^{-14}$–10^{-13} s. In asymmetric doped bilayer [Figs. 12(d) and 12(c)] similar effect occurs at energies with small Boltzmann velocity (Fig. 7). This regime, called small velocity regime, where non-Boltzmann terms dominate transport properties, has already been observed in

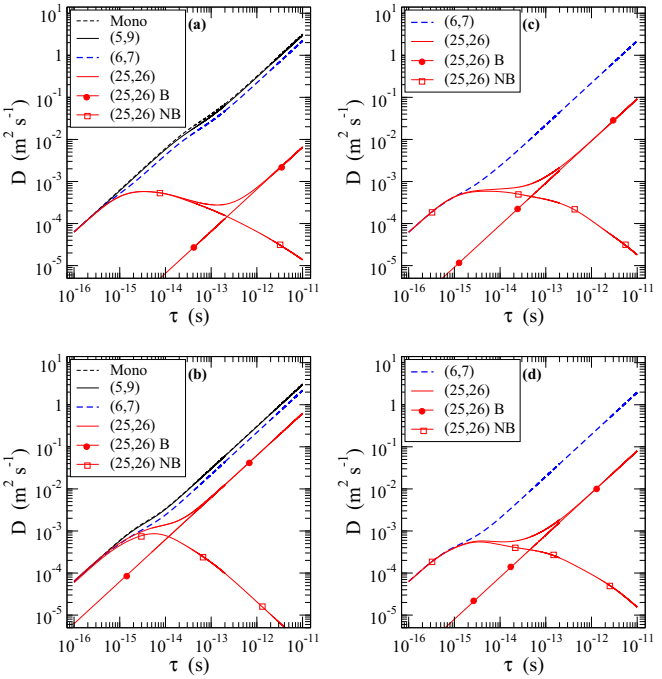

FIG. 12. Diffusivity D versus scattering time τ in graphene (5,9), (6,7), and (25,26) bilayers. For (25,26) bilayers, the Boltzmann (B) term and non-Boltzmann (NB) term are shown. $\Delta\epsilon = 0$ for (a) energy $E_{\rm F}$ close to the Dirac energy ($E_D = 0$), (b) $E_{\rm F} = 0.1$ eV. (c) $\Delta\epsilon = 0.2$ and $E_{\rm F} = -0.1$ eV, (d) $\Delta\epsilon = 0.6$ and $E_{\rm F} = -0.3$ eV.

systems with complex atomic structure such as quasicrystals and complex metallic alloys (see Refs. [35–37,46,47] and references therein). Roughly speaking, small velocity regime is reached when mean-free path $l = V\tau$ of charge carriers is smaller than spatial extension L_{wp} of the corresponding wave packet. In this case, semiclassical approximation breaks down and a pure quantum description is necessary to calculated transport properties. Twisted bilayer with very small rotation angle have a huge unit cell and a huge cell of the moiré, in which states at $E \simeq E_D$ are confined in the AA zone [24] and have then a very small velocity (Fig. 7). Typically, the size of the AA zone is $\sim 0.5P$, where P is the moiré period [Eq. (5)], and then the extension of confined states in the AA zone is $L_{wp} \lesssim 0.5P$. As P increases when θ increases, the condition $V\tau < L_{wp}$ of the small velocity regime should be satisfied for θ small enough.

In doped and undoped twisted bilayers, for energy which does not correspond to the a peak of localization in the DOS, the Boltzmann velocity is larger, and the non-Boltzamnn effect is neglectable [Fig. 12(b)].

VIII. CONCLUSION

To sum up, numerical calculations show that doped rotated layers with large rotation angle and reasonable doping (inducing a shift of the Dirac point smaller than 0.8 eV) still behave like decoupled layers as found experimentally [34]. This result is of particular importance for epitaxial graphene on the C face of SiC, at least for large rotation angles. In this case, the C plane closest to the interface dominates the

transport because it is doped due to charge transfer from the interface. This charge transfer corresponds to a shift of the Dirac point of 0.2–0.3 eV above the Fermi level. Experiments and theory [48] showed that it is decoupled from the substrate and thanks to a large rotation angle stacking, it can also be decoupled from the other C planes. Here, we show that actual asymmetric doping does not alter the layer decoupling so that this plane can exhibit isolated graphene like properties even if it is sandwiched between the interface and other C layers as observed experimentally [49,50].

Thanks to the tight-binding scheme, we have been able to address the important question of the effect of doping on rotated graphene bilayers with intermediate angle values corresponding to large cells of moiré. For a small symmetric doping, twisted layers with large and intermediate rotation angles keep their characteristics: linear band dispersions, renormalized band velocity at Dirac point (K point), and van Hove singularities, as expected experimentally [34]. But, a large enough doping increases the renormalization of the velocity. For large angles, this new effect occurs for unphysical doping values, but for intermediate angles, it occurs for accessible doping values, typically when $\Delta\epsilon =$ few 0.1 eV.

For very small angles, electronic states remain confined in the AA region of the moiré whatever the doping is, as in undoped bilayers [23,24]. Therefore, the regime of confinement by very large cells of the moiré is not destroyed by the doping, but localization energies are shifted with the doping rate. In this latter case, by conductivity calculations, we show that the Bloch-Boltzmann model breaks down and strong interference quantum effects dominate transport properties.

ACKNOWLEDGMENTS

The authors wish to thank P. Mallet, J.-Y. Veuillen, V. Cherkez, C. Berger, and W. A. de Heer for fruitful discussions. The numerical calculations have been performed at the Centre de Calculs (CDC), Université de Cergy-Pontoise. We thank Y. Costes and D. Domergue, CDC, for computing assistance. We acknowledge financial support from Grant No. ANR-15-CE24-0017.

APPENDIX: QUANTUM TRANSPORT CALCULATION

1. Average square spreading in perfect crystal at zero temperature

In the framework of the Kubo-Greenwood approach for calculation of the conductivity, a central quantity is the average quadratic spreading of wave packets of energy E at time t along the x direction [35,36,43,44,51–53]

$$\Delta X^2(E,t) = \langle (\hat{X}(t) - \hat{X}(0))^2 \rangle_E, \tag{A1}$$

where $\hat{X}(t)$ is the Heisenberg representation of the position operator $\hat{X}$. $\langle \hat{A} \rangle_E$ means an average of diagonal elements of the operator $\hat{A}$ over all states with energy E. The diffusivity at zero temperature $\mathcal{D}(E)$ at energy E is deduced from ΔX^2,

$$\mathcal{D}(E) = \lim_{t \to +\infty} D(E,t), \tag{A2}$$

with

$$D(E,t) = \frac{\Delta X^2(E,t)}{t}, \tag{A3}$$

where $D(E,t)$ is called diffusion coefficient. In a two-dimensional system with surface S, the dc conductivity σ_{xx} at zero temperature along the x direction is given by the Einstein formula

$$\sigma_{xx}(E_F) = \frac{e^2}{S} n(E_F) \mathcal{D}(E_F), \tag{A4}$$

where $n(E)$ is the total density of states per S and E_F the Fermi energy.

In pure crystals at zero temperature, once the band structure is calculated from the tight-binding Hamiltonian, the average quadratic spreading can be computed exactly in the basis of Bloch states [35,43]. The average square spreading is the sum of two terms [35,43]:

$$\Delta X^2(E,t) = V_B^2 t^2 + \Delta X^2_{NB}(E,t). \tag{A5}$$

The first term is the ballistic (intraband) contribution at the energy E. V_B is the Boltzmann velocity in the x direction. The semiclassical theory is equivalent to taking into account only this first term. The second term (interband contributions) $\Delta X^2_{NB}(E,t)$ is a nonballistic (non-Boltzmann) contribution. It is due to the nondiagonal elements in the eigenstates basis $\{|n\rangle\}$ of the velocity operator $\hat{V}_x$:

$$\hat{V}_x = \frac{1}{i\hbar}[\hat{X}, \hat{H}]. \tag{A6}$$

From the definition (A1), one obtains [43]

$$\Delta X^2_{NB}(E,t) = 2\hbar^2 \left\langle \sum_{\vec{k},n'(n' \neq n)} \left[1 - \cos\left(\frac{(E_{\vec{k},n} - E_{\vec{k},n'})t}{\hbar} \right) \right] \times \frac{|\langle n\vec{k}|\hat{V}_x|n'\vec{k}\rangle|^2}{(E_{\vec{k},n} - E_{\vec{k},n'})^2} \right\rangle_{E_{\vec{k},n}=E}, \tag{A7}$$

where $E_{\vec{k},n}$ is the energy of the eigenstate $|n\vec{k}\rangle$ computed by diagonalization of the tight-binding Hamiltonian in reciprocal space. The average velocity, i.e., Boltzmann velocity, along direction x of the electrons at energy E is obtained numerically from diagonal elements of $\hat{V}_x$:

$$V_B(E) = \sqrt{\langle |\langle n\vec{k}|\hat{V}_x|n\vec{k}\rangle|^2 \rangle_{E_{\vec{k},n}=E}}. \tag{A8}$$

2. Relaxation time approximation

The effect of static disorder and/or decoherence mechanisms such as electron-electron scattering, electron phonon interaction (temperature), is not considered in the above section. This effect can be treated in a phenomenological way by introducing an inelastic scattering time τ in the relaxation time approximation (RTA) [35]. τ may include elastic scattering time τ_e (due to static defects such as vacancies or adatoms) and inelastic scattering time τ_i (due to phonon, electron-electron scattering, effect of magnetic field): $\tau^{-1} = \tau_e^{-1} + \tau_i^{-1}$. τ decreases when the temperature increases and/or static defects concentration increases. In actual graphene at

room temperature, realistic values of τ_i are a few 10^{-13} s [45]. The conductivity can then be estimated by

$$\sigma_{xx}(E_{\rm F},\tau) = \frac{e^2}{S} n(E_{\rm F}) \mathcal{D}(E_{\rm F},\tau), \tag{A9}$$

with diffusivity

$$D(E_{\rm F},\tau) = \frac{1}{2\tau^2} \int_0^\infty \Delta X^2(E_{\rm F},t)\, e^{-t/\tau}\, dt\,, \tag{A10}$$

where $\Delta X^2(E,t)$ is the average square spreading in crystal without defects [Eq. (A1)]. Here, the Fermi-Dirac distribution function is taken equal to its zero-temperature value. This is valid provided that the electronic properties vary smoothly on the thermal energy scale $k_{\rm B}T$. From Eqs. (A5) and (A10), D is the sum of a Boltzmann contribution $D_{\rm B}$ and a non-Boltzmann contribution $D_{\rm NB}$:

$$\mathcal{D}(E_{\rm F},\tau) = \mathcal{D}_{\rm B}(\tau) + \mathcal{D}_{\rm NB}(E_{\rm F},\tau). \tag{A11}$$

RTA has been used successfully to compute [35] conductivity in approximants of quasicrystals where quantum diffusion and localization effect play an essential role [35–37,54,55] and conductivity in organic semiconductors [56]. In this paper, we show that quantum interferences have also a strong effect in transport properties of rotated bilayers with very small angles.

3. Quantum transport in graphene

In pure graphene, assuming a restriction of the Hamiltonian [Eq. (1)] to the first-neighbor interactions only, $\Delta X^2_{\rm NB}(E,t)$ is given by

$$\Delta X^2_{\rm NB}(E,t) = \frac{V_B^2\hbar^2}{2E^2}\left(1 - \cos\frac{2E}{\hbar}t\right), \tag{A12}$$

with

$$V_{\rm B} = \frac{3a\gamma_0}{2\sqrt{2}\hbar}, \tag{A13}$$

where γ_0 is the coupling term between first-neighbor p_z orbitals. At small time t, $t \ll \hbar/E$, the non-Boltzmann term is equal to Boltzmann term $\Delta X^2_{\rm NB}(E,t) \simeq V_{\rm B}^2 t^2$, thus $\Delta X^2(E,t) \simeq 2V_{\rm B}^2 t^2$ and $D(E,t) \simeq 2V_{\rm B}^2 t$. Whereas for large t, the Boltzmann term dominates and $\Delta X^2(E,t) \simeq V_{\rm B}^2 t^2$ and $D(E,t) \simeq V_{\rm B}^2 t$. The non-Boltzmann term is due to matrix elements of the velocity operator between the two bands (i.e., interband coupling between the hole and electron states having the same wave vector). These matrix elements imply that the velocity correlation function has also two parts: one constant and the other oscillating at a frequency $2E/\hbar$ where E is the energy of the state. This is precisely the phenomenon of jittery motion also called Zitterbewegung. Note that in any crystal having several bands there are also components of the velocity correlation function which are oscillating at frequencies $(E_{\vec{k},n} - E_{\vec{k},n'})/\hbar$. Therefore, Zitterbewegung is quite common in condensed matter physics. For example, approximants of quasicrystals present very strong Zitterbewegung effect and the non-Boltzmann contribution dominates the Boltzmann contribution [35,37,46,47].

With defects (static defects or phonons ...) in RTA, the diffusivity $\mathcal{D}(E_{\rm F},\tau)$ is also the sum of a Boltzmann term

$$\mathcal{D}_{\rm B}(\tau) = \tfrac{1}{3} V_B^2 \tau \tag{A14}$$

and a non-Boltzmann term

$$\mathcal{D}_{\rm NB}(E_{\rm F},\tau) = \frac{1}{3} V_B^2 \tau \left(\frac{\hbar^2}{\hbar^2 + 4E_{\rm F}^2\tau^2}\right). \tag{A15}$$

For small scattering time $\tau \ll \hbar/E$, the non-Boltzmann term $\mathcal{D}_{\rm NB}$ is equal to Boltzmann term $\mathcal{D}_{\rm B}$ and $\mathcal{D} = 2\mathcal{D}_{\rm B}$. For large τ, $\tau \gg \hbar/E$, $\mathcal{D}_{\rm NB} \to 0$ and $\mathcal{D} = \mathcal{D}_{\rm B}$. When $E_{\rm F} = 0$ (i.e., Dirac energy), the non-Boltzmann term equals the Boltzmann term for all scattering times. On Figs. 12(a) and 12(b), this modification of $\mathcal{D}(\tau)$ at $\tau = \hbar/E$ is clearly seen. But, this limit case should be very difficult to obtain experimentally. Similar results are obtained for twisted bilayers with large angle of rotation θ, whereas for small θ this modification becomes larger showing that the non-Boltzmann term is not neglectable anymore.

[1] P. R. Wallace, The band theory of graphite, Phys. Rev. **71**, 622 (1947).

[2] C. Berger, Z. M. Song, X. B. Li, X. S. Wu, N. Brown, C. Naud, D. Mayou, T. B. Li, J. Hass, A. N. Marchenkov, E. H. Conrad, P. N. First, and W. A. de Heer, Electronic confinement and coherence in patterned epitaxial graphene, Science **312**, 1191 (2006).

[3] A. H. Castro Neto, F. Guinea, N. M. R. Peres, K. S. Novoselov, and A. K. Geim, The electronic properties of graphene, Rev. Mod. Phys. **81**, 109 (2009).

[4] S. Latil and L. Henrard, Charge Carriers in Few-Layer Graphene Films, Phys. Rev. Lett. **97**, 036803 (2006).

[5] F. Zhang, B. Sahu, H. Min, and A. H. MacDonald, Band structure of ABC-stacked graphene trilayers, Phys. Rev. B **82**, 035409 (2010).

[6] F. Varchon, P. Mallet, J.-Y. Veuillen, and L. Magaud, Ripples in epitaxial graphene on the Si-terminated SiC(0001) surface, Phys. Rev. B **77**, 235412 (2008).

[7] T. Ohta, A. Bostwick, T. Seyller, K. Horn, and E. Rotenberg, Controlling the electronic structure of bilayer graphene, Science **313**, 951 (2006).

[8] I. Brihuega, P. Mallet, C. Bena, S. Bose1, C. Michaelis, L. Vitali, F. Varchon, L. Magaud, K. Kern, and J. Y. Veuillen, Quasiparticle Chirality in Epitaxial Graphene Probed at the Nanometer Scale, Phys. Rev. Lett. **101**, 206802 (2008).

[9] J. Hass, W. A. de Heer, and E. H. Conrad, The growth and morphology of epitaxial multilayer graphene, J. Phys.: Condens. Matter **20**, 323202 (2008).

[10] K. V. Emtsev, F. Speck, Th. Seyller, L. Ley, and J. D. Riley, Interaction, growth, and ordering of epitaxial graphene on SiC0001 surfaces: A comparative photoelectron spectroscopy study, Phys. Rev. B **77**, 155303 (2008).

[11] F. Varchon, P. Mallet, L. Magaud, and J.-Y. Veuillen, Rotational disorder in few-layer graphene lms on 6H-SiC(000-1): A

scanning tunneling microscopy study, Phys. Rev. B **77**, 165415 (2008).

[12] M. Sprinkle, D. Siegel, Y. Hu, J. Hicks, A. Tejeda, A. Taleb-Ibrahimi, P. Le Fèvre, F. Bertran, S. Vizzini, H. Enriquez, S. Chiang, P. Soukiassian, C. Berger, W. A. de Heer, A. Lanzara, and E. H. Conrad, First Direct Observation of a Nearly Ideal Graphene Band Structure, Phys. Rev. Lett. **103**, 226803 (2009).

[13] S. Latil, V. Meunier, and L. Henrard, Massless fermions in multilayer graphitic systems with misoriented layers: Ab initio calculations and experimental fingerprints, Phys. Rev. B **76**, 201402(R) (2007).

[14] J. M. B. Lopez dos Santos, N. M. R. Peres, and A. H. Castro Neto, Graphene Bilayer with a Twist: Electronic Structure, Phys. Rev. Lett. **99**, 256802 (2007).

[15] S. Shallcross, S. Sharma, and O. A. Pankratov, Quantum Interference at the Twist Boundary in Graphene, Phys. Rev. Lett. **101**, 056803 (2008).

[16] S. Shallcross, S. Sharma, E. Kandelaki, and O. A. Pankratov, Electronic structure of turbostratic graphene, Phys. Rev. B **81**, 165105 (2010).

[17] R. Bistritzer and A. H. MacDonald, Transport between twisted graphene layers, Phys. Rev. B **81**, 245412 (2010).

[18] R. Bistritzer and A. H. MacDonald, Moiré butteries in twisted bilayer graphene, Phys. Rev. B **84**, 035440 (2011).

[19] R. Bistritzer and A. H. MacDonald, Moiré bands in twisted double-layer graphene, Proc. Natl. Acad. Sci. USA **108**, 12233 (2011).

[20] E. J. Mele, Commensuration and interlayer coherence in twisted bilayer graphene, Phys. Rev. B **81**, 161405(R) (2010).

[21] E. J. Mele, Band symmetries and singularities in twisted multilayer graphene, Phys. Rev. B **84**, 235439 (2011).

[22] E. Suarez Morell, J. D. Correa, P. Vargas, M. Pacheco, and Z. Barticevic, Flat bands in slightly twisted bilayer graphene: Tight-binding calculations, Phys. Rev. B **82**, 121407(R) (2010).

[23] G. Trambly de Laissardière, D. Mayou, and L. Magaud, Localization of dirac electrons in rotated graphene bilayers, Nano Lett. **10**, 804 (2010).

[24] G. Trambly de Laissardière, D. Mayou, and L. Magaud, Numerical studies of confined states in rotated bilayers of graphene, Phys. Rev. B **86**, 125413 (2012).

[25] J. M. B. Lopes dos Santos, N. M. R. Peres, and A. H. Castro Neto, Continuum model of the twisted graphene bilayer, Phys. Rev. B **86**, 155449 (2012).

[26] E. Suárez Morell, M. Pacheco L. Chico, and L. Brey, Electronic properties of twisted trilayer graphene, Phys. Rev. B **87**, 125414 (2013).

[27] O. Faizy Namarvar, G. Trambly de Laissardière, and D. Mayou, Electron coupling and density of states in rotated bilayer graphene, arXiv:1402.5879.

[28] K. Uchida, S. Furuya, J.-I. Iwata, and A. Oshiyama, Atomic corrugation and electron localization due to Moiré patterns in twisted bilayer graphenes, Phys. Rev. B **90**, 155451 (2014).

[29] W. Landgraf, S. Shallcross, K. Türschmann, D. Weckbecker, and O. Pankratov, Electronic structure of twisted graphene flakes, Phys. Rev. B **87**, 075433 (2013).

[30] A. O. Sboychakov, A. L. Rakhmanov, A. V. Rozhkov and F. Nori, Electronic spectrum of twisted bilayer graphene, Phys. Rev. B **92**, 075402 (2015).

[31] G. Li, A. Luican, L. M. B. Lopes dos Santos, A. H. Castro Neto, A. Reina, J. Kong, and E. Y. Andrei, Observation of Van Hove singularities in twisted graphene layers, Nat. Phys. **6**, 109 (2010).

[32] A. Luican, G. Li, A. Reina, J. Kong, R. R. Nair, K. S. Novoselov, A. K. Geim, and E. Y. Andrei, Single-layer Behavior and its Breakdown in Twisted Graphene Layers, Phys. Rev. Lett. **106**, 126802 (2011).

[33] I. Brihuega, P. Mallet, H. González-Herrero, G. Trambly de Laissardière, M. M. Ugeda, L. Magaud, J. M. Gómez-Rodríguez, F. Ynduráin, and J.-Y. Veuillen, Unravelling the Intrinsic and Robust Nature of van Hove Singularities in Twisted Bilayer Graphene, Phys. Rev. Lett. **109**, 196802 (2012).

[34] V. Cherkez, G. Trambly de Laissardière, P. Mallet, and J.-Y. Veuillen, Van Hove singularities in doped twisted graphene bilayers studied by Scanning Tunneling Spectroscopy, Phys. Rev. B **91**, 155428 (2015).

[35] G. Trambly de Laissardière, J.-P. Julien, and D. Mayou, Quantum Transport of Slow Charge Carriers in Quasicrystals and Correlated Systems, Phys. Rev. Lett. **97**, 026601 (2006).

[36] G. Trambly de Laissardière and D. Mayou, Anomalous electronic transport in Quasicrystals and related Complex Metallic Alloys, C. R. Phys. **15**, 70 (2014).

[37] G. Trambly de Laissardière, A. Szállás, and D. Mayou, Electronic structure and transport in approximants of the Penrose tiling, Acta Phys. Pol. **126**, 617 (2014).

[38] J. C. Slater and G. F. Koster, Simplified LCAO method for the periodic potential problem, Phys. Rev. **94**, 1498 (1954).

[39] S. Roche and D. Mayou, Conductivity of Quasiperiodic Systems: A Numerical Study, Phys. Rev. Lett. **79**, 2518 (1997).

[40] J. M. Campanera, G. Savini, I. Suarez-Martinez, and M. I. Heggie, Density functional calculations on the intricacies of Moiré patterns on graphite, Phys. Rev. B **75**, 235449 (2007).

[41] E. McCann, Asymmetry gap in the electronic band structure of bilayer graphene, Phys. Rev. B **74**, 161403(R) (2006).

[42] Y. Kim, H. Yun, S.-G. Nam, M. Son, D. S. Lee, D. C. Kim, S. Seo, H. C. Choi, H.-J. Lee, S. W. Lee, and J. S. Kim, Breakdown of the Interlayer Coherence in Twisted Bilayer Graphene, Phys. Rev. Lett. **110**, 096602 (2013).

[43] D. Mayou and G. Trambly de Laissardière, in *Quasicrystals, Series Handbook of Metal Physics*, edited by T. Fujiwara and Y. Ishii (Elsevier, Amsterdam, 2008), p. 209–265.

[44] D. Mayou, Generalized Drude Formula for the Optical Conductivity of Quasicrystals, Phys. Rev. Lett. **85**, 1290 (2000).

[45] X. Wu, X. Li, Z. Song, C. Berger, and W. A. de Heer, Weak Antilocalization in Epitaxial Graphene: Evidence for Chiral Electrons, Phys. Rev. Lett. **98**, 136801 (2007).

[46] F. Triozon, J. Vidal, R. Mosseri, and D. Mayou, Quantum dynamics in two- and three-dimensional quasiperiodic tilings, Phys. Rev. B **65**, 220202 (2002).

[47] G. Trambly de Laissardière, C. Oguey, and D. Mayou, Breakdown of semi-classical conduction theory in approximants of the octagonal tiling, Philos. Mag. **91**, 2778 (2011).

[48] L. Magaud, F. Hiebel, F. Varchon, P. Mallet, and J.-Y. Veuillen, Graphene on the C-terminated SiC $(000\bar{1})$ surface: An *ab initio* study, Phys. Rev. B **79**, 161405(R) (2009).

[49] M. L. Sadowski, G. Martinez, M. Potemski, C. Berger, and W. A. de Heer, Landau Level Spectroscopy of Ultrathin Graphite Layers, Phys. Rev. Lett. **97**, 266405 (2006).

[50] J. Hass, F. Varchon, J. E. Millan-Otoya, M. Sprinkle, N. Sharma, W. A. de Heer, C. Berger, P. N. First, L. Magaud, and E. H. Conrad, Why Multilayer Graphene on 4H-SiC(000$\bar{1}$) Behaves Like a Single Sheet of Graphene? Phys. Rev. Lett. **100**, 125504 (2008).

[51] D. Mayou, Calculation of the conductivity in the short-mean-free-path regime, Europhys. Lett. **6**, 549 (1988).

[52] S. Roche and D. Mayou, Formalism for the computation of the RKKY interaction in aperiodic systems, Phys. Rev. B **60**, 322 (1999).

[53] D. Mayou and S. N. Khanna, A real-space approach to electronic transport, J. Phys. I (Paris) **5**, 1199 (1995).

[54] C. Berger, E. Belin, and D. Mayou, Electronic properties of quasicrystals, Ann. Chim. Mater. (Paris) **18**, 485 (1993).

[55] E. Belin and D. Mayou, Electronic properties of Quasicrystals, Phys. Scr., T **49A**, 356 (1993).

[56] S. Ciuchi, S. Fratini, and D. Mayou, Transient localization in crystalline organic semiconductors, Phys. Rev. B **83**, 081202(R) (2011).